ACS APPLIED MATERIALS & INTERFACES

Research Article

www.acsami.org

Enhanced Supercapacitive Performance of Chemically Grown Cobalt–Nickel Hydroxides on Three-Dimensional Graphene Foam Electrodes

Umakant M. Patil,[§,†] Ji Soo Sohn,[§,†] Sachin B. Kulkarni,[†] Su Chan Lee,[†] Hyung Goo Park,[†] Kishor V. Gurav,[‡] J.H. Kim,[‡] and Seong Chan Jun*[,†]

[†]Nano ElectroMechanical Device Laboratory, School of Mechanical Engineering, Yonsei University, Seoul 120-749, South Korea

[‡]Department of Materials Science and Engineering, Chonnam National University, Gwangju 500-757, South Korea

Supporting Information

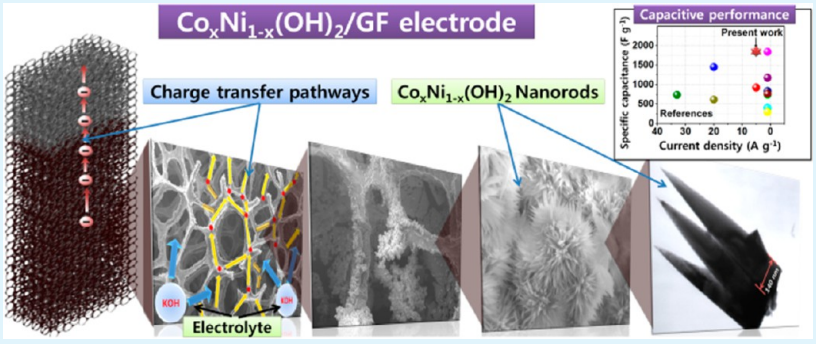

ABSTRACT: Chemical growth of mixed cobalt–nickel hydroxides ($Co_xNi_{1-x}(OH)_2$), decorated on graphene foam (GF) with desirable three-dimensional (3D) interconnected porous structure as electrode and its potential energy storage application is discussed. The nanostructured $Co_xNi_{1-x}(OH)_2$ films with different Ni:Co (x) compositions on GF are prepared by using the chemical bath deposition (CBD) method. The structural studies (X-ray diffraction and X-ray photoelectron spectroscopy) of electrodes confirm crystalline nature of $Co_xNi_{1-x}(OH)_2$/GF and crystal structure consists of $Ni(OH)_2$ and $Co(OH)_2$. The morphological properties reveal that nanorods of $Co(OH)_2$ reduce in size with increases in nickel content and are converted into $Ni(OH)_2$ nanoparticles. The electrochemical performance reveals that the $Co_{0.66}Ni_{0.33}(OH)_2$/GF electrode has maximum specific capacitance of ~1847 F g^{-1} in 1 M KOH within a potential window 0 to 0.5 V vs Ag/AgCl at a discharge current density of 5 A g^{-1}. The superior pseudoelectrochemical properties of cobalt and nickel are combined and synergistically reinforced with high surface area offered by a conducting, porous 3D graphene framework, which stimulates effective utilization of redox characteristics and communally improves electrochemical performance with charge transport and storage.

KEYWORDS: *$Co_xNi_{1-x}(OH)_2$/GF, nanorods, supercapacitor, energy and power density*

1. INTRODUCTION

Nowadays, there has been need to design and construct energy storage devices (supercapacitors) that can provide high energy and power to accomplish emerging demand of portable electronic devices.[1−5] Generally, in supercapacitors, energy can be store by either ion adsorption (electrochemical double layer capacitors, EDLCs) or surface redox reactions (pseudocapacitors). However, supercapacitors based on EDLC exhibits low specific capacitance (SC), which cannot meet the emerging requirements for devices that need high energy and power. Subsequently, there has been growing interest in pseudocapacitive materials for supercapacitors with high energy density, which is larger at least by one magnitude than EDLCs.[1−6]

Generally, metal hydroxides/oxides and conductive polymers with multiple oxidation states, which possess a redox reaction, are used as pseudocapacitive materials.[7,8] Among many metal oxides/hydroxides, $Co(OH)_2$ and $Ni(OH)_2$ are the best candidates as a pseudocapacitive electrode material with very high specific capacitances, owing to their layered structures with large interlayer spacing and characteristic redox reaction.[9,10] Mixed metal hydroxide [$Co_xNi_{1-x}(OH)_2$] is advantageous in terms of environmental friendliness, low cost, and abundance in nature; therefore, it is considered a promising lucrative pseudocapacitive material in supercapacitors.[11−13] It has been reported that the $Co_xNi_{1-x}(OH)_2$ demonstrates improved electrical conductivity along with electrochemical activity than solitary nickel hydroxide or cobalt hydroxide.[13] Consequently, it is expected that $Co_xNi_{1-x}(OH)_2$ offers more affluent redox reactions, including contributions from both nickel and cobalt ions, than those of the solitary nickel hydroxide and cobalt

Received: November 1, 2013
Accepted: February 4, 2014
Published: February 4, 2014

   dx.doi.org/10.1021/am404863z | ACS Appl. Mater. Interfaces 2014, 6, 2450−2458

hydroxide. These remarkable characteristics of mixed metal hydroxides pronounce its benefits and promotes their use in a high performance supercapacitor application. A maximum specific capacitance of 1809 F g^{-1} in 6 M KOH electrolyte is reported by Hu et al. for Co_xNi_{1-x} LDHs prepared using chemical coprecipitation method with polyethylene glycol as complexing agent.[14] Kulkarni et al. reported maximal specific capacitance of 1213 F g^{-1} for electrochemically deposited Co_xNi_{1-x}LDHs on stainless steel by potentiodynamic mode.[15]

In general, to maximize the supercapacitance of pseudocapacitive material, it is crucial to construct electrodes with a substantial amount of electroactive sites and easy transport paths for both electrolyte ions and electrons in redox reactions.[16−18] In efforts to improve electrochemical performance of $Co_xNi_{1-x}(OH)_2$ based supercapacitor electrodes, its various nanostructures and composites with carbon material (comprising high-surface-area with good conductivity) have been studied.[19−21] In such composite materials, carbon based materials play an important role with the intention of proficient charge transport, by enhancing the electrical conductivity along with shortening electron and ion diffusion pathways.[21] However, such composites need to be coated on a metal current collector to find a continuous conductive structure, which drastically decreases the inclusive specific capacitance. The $Co_xNi_{1-x}(OH)_2$ based electrodes are usually binder-enriched electrodes prepared by the conventional slurry-coating technique.[22] Consequently, addition of polymeric binder reduces the inclusive supercapacitive performance by impeding the charge transport rate and increasing the total mass of the electrode. The three-dimensional (3D) nickel foam is generally used as a substrate for supercapacitor electrode fabrication. The considerable weight of the nickel foam (density of ∼262 mg cm^{-3}) ensured the decrease in the gravimetric capacitance (with respect to inclusive weight of the electrode). Recently, a lightweight graphene foam (GF) (low density of ∼20 mg cm^{-3}), a foam structure containing ultrathin graphene skeleton, was used as a current collector, which provides the free-standing 3D interconnected network with high electrical conductivity.[23−25] Properties like continuous conducting structure and being lightweight make GF a promising candidate as a substitute to conventional current collectors such as nickel foam or carbon paper.[23]

On the basis of the above considerations, here we report a fabrication of binder-free $Co_xNi_{1-x}(OH)_2$/GF composite electrode by direct growth of a porous $Co_xNi_{1-x}(OH)_2$ nanorods on the GF surface by chemical bath deposition (CBD) method and its improved supercapacitor performance. The influence of composition variation of Co and Ni on structural, morphological and supercapacitive properties of $Co_xNi_{1-x}(OH)_2$ are investigated in terms of specific capacitance, energy and power density. The obtained results will help to amend and construct $Co_xNi_{1-x}(OH)_2$/GF electrodes according to energy storage applications.

2. EXPERIMENTAL SECTION

The fabrication of self-supported $Co_xNi_{1-x}(OH)_2$ on 3D graphene foam consists of a two step procedure. The first step is preparation of the GF, which includes the growth of graphene on Ni foam using the chemical vapor deposition (CVD) method, followed by etching of Ni foam through etchant; the details of this process are described in ref 24 and a schematic is shown in Figure S1 (see the Supporting Information). The second step is the preparation of $Co_xNi_{1-x}(OH)_2$ on GF by the CBD method. Typically, 0.1 M $Ni(NO_3)_2.6H_2O$, 0.1 M $Co(NO_3)_2{\cdot}6H_2O$ and 0.25 M $CO(NH_2)_2$ were dissolved in 50 mL of deionized water with magnetic stirring for 10 min to form a homogeneous solution. The different compositions of $Co_xNi_{1-x}(OH)_2$ were prepared from various $Co(NO_3)_2$:$Ni(NO_3)_2$ weight ratios 'x' as 1.0:0.0, 0.66:0.33, 0.50:0.50, 0.33:0.66 and 0.0:1.0. A piece of GF (2 × 4 cm^2) was placed vertically, with the support of glass microslide, in the prepared solution. The bath was sealed and placed in a vessel containing paraffin oil for constant heating. The temperature of the system was maintained, without stirring, at 120 °C for 4 h and then allowed to cool down to room temperature spontaneously. After the reaction, samples were rinsed with distilled water several times to remove the residual reactants. The weights of deposited materials were determined gravimetrically by measuring the change in weight of the GF before and after the material deposition. The graph of materials weights with different composition is shown in Figure S2 (see the Supporting Information).

The electrode materials were structurally characterized by X-ray diffraction (XRD), field-emission scanning electron microscopy (FESEM), transmission electron microscopy (TEM) and X-ray photoelectron spectroscopy (XPS) measurements. XRD was carried out on a Rigaku Ultima diffractometer using Cu Kα radiation. The morphology of the composite was examined by field-emission scanning electron microscopy (FESEM, JSM-7001F, JEOL). XPS measurements were carried out on a thermo scientific ESCALAB 250 (Thermo Fisher Scientific, UK). Supercapacitor performance was studied by forming a conventional half-test cell, containing a three-electrode system with $Co_xNi_{1-x}(OH)_2$/GF as the working electrode, Ag/AgCl as reference electrode and platinum (Pt) as counter electrode in a 1 M KOH aqueous electrolyte. Cyclic voltammetry (CV), galvanostatic charge/discharge tests and EIS measurements were performed using ZIVE SP2 LAB analytical equipment (South Korea).

3. RESULTS AND DISCUSSION

3.1. Film Formation and Reaction Mechanism. Synthesis of $Co_xNi_{1-x}(OH)_2$ on GF was achieved by using the CBD method. The CBD method is one of the efficient "bottom-up" approaches to grow nanostructures; it is based on the formation of a solid phase from solution, which involves three collective steps: nucleation, coalescence and particle growth.[26]

To account, formation of $Co_xNi_{1-x}(OH)_2$ nanorods on GF and their robust adhesion, we present the schematic of the growth mechanism in Figure 1. The crystal formation process of the precursor can be classified as heterogeneous nucleation and subsequent crystal growth. If only crystal seeds are produced on the heterogeneous substrate, the subsequent growth of a porous film will be feasible. During the preparation of graphene on Ni foam by the CVD method, the mechanism allows the formation of some wrinkles on the surface of the graphene skeleton due to grain boundaries of Ni. Carboxyl, hydroxyl and epoxy groups were obtained on the graphene surface during Ni foam etching. Such wrinkles, carboxyl, hydroxyl and epoxy groups on the graphene skeleton are favorable for the nucleation of crystal seeds (step I).

In the formation $Co_xNi_{1-x}(OH)_2$, as the temperature of solution bath increased to 120 °C, decomposition of urea (reaction 1) took place, producing CO_2 and NH_3 gradually.[27]

$$NH_2CONH_2 + H_2O \xrightarrow{\Delta} 2NH_3 + CO_2 \quad (1)$$

After decomposition of urea, as per the above reaction, the solution became alkaline; such an alkaline condition is more favorable to generate more carboxyl, hydroxyl and epoxy group on graphene surface. Increased carboxyl, hydroxyl and epoxy groups are constructed in order to create more nucleation sites (step II).

Simultaneously, Ni^{2+} and Co^{2+} from $Ni(NO_3)_2$ and $Co(NO_3)_2$ get mixed with NH_3, which formed amine complex. Such amine complexed metal ions easily get adsorbed on the heterogeneous surface of the substrate by electrostatic or van der Waals force

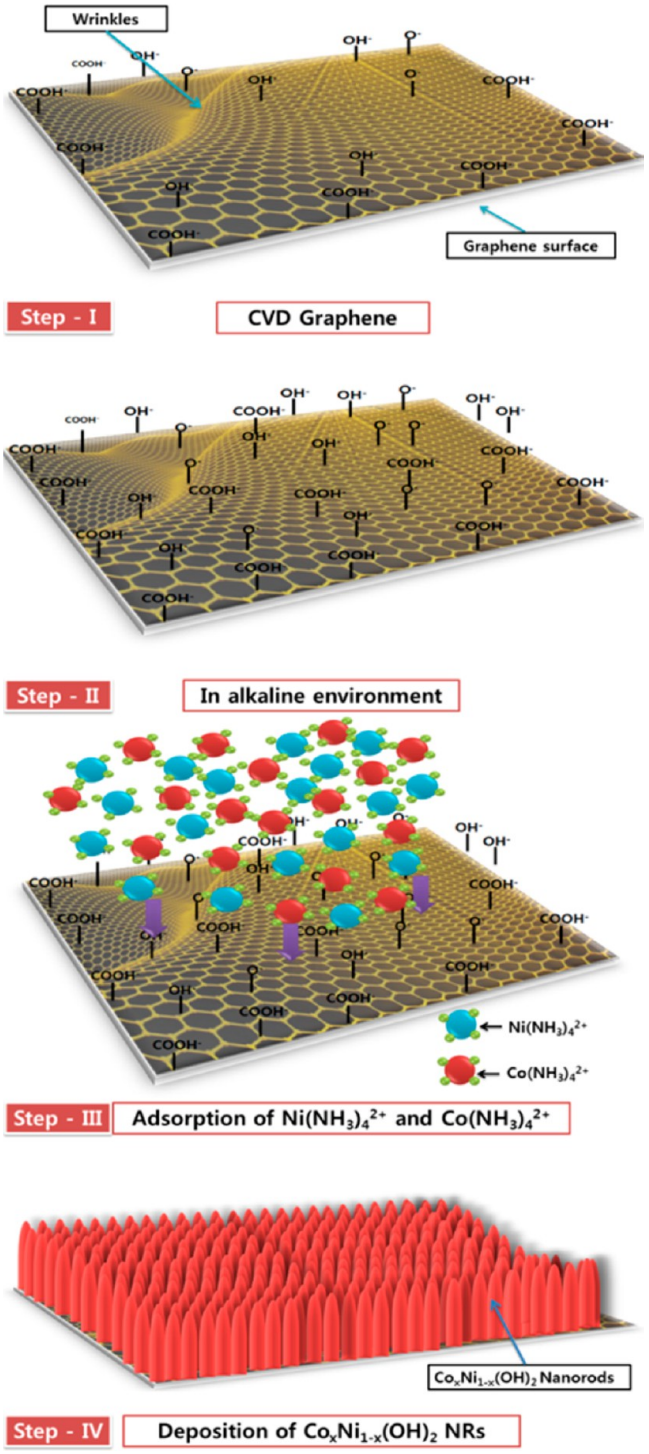

Figure 1. Schematic of growth mechanism of formation of $Co_xNi_{1-x}(OH)_2$ Nanorods on GF. Step I: CVD graphene skeleton with some wrinkles along with some attached carbo-hydroxyl group on the surface during etching process. Step II: favorable alkaline condition to more carbo-hydroxyle group to form on graphene surface for nucleation. Step III: adsorption of metal (Ni, Co) amine complex on the heterogeneous surface of the substrate. Step IV: consequent growth of $Co_xNi_{1-x}(OH)_2$ nanorods.

(step III). The high specific surface area of GF makes it easy to adsorb a large number of amine complexed Ni^{2+} and Co^{2+}.

$$Ni^{2+} + NH_3 \rightarrow Ni(NH_3)_4{}^{2+} \quad (2)$$

$$Co^{2+} + NH_3 \rightarrow Co(NH_3)_4{}^{2+} \quad (3)$$

Initially, the solution was neutral with pH about ~6−7 and then increased gradually and monotonically with time and temperature, the solution became alkalescent. At this alkalescent bath condition, the $Ni(NH_3)_4{}^{2+}$ and $Co(NH_3)_4^{2+}$ is instable and the following reactions occur to form mixed metal hydroxides on the graphene surface in form of nanorods (step IV):

$$Ni[(NH)_3]_4^{2+} + 2OH^- \rightarrow Ni(OH)_2 + 4NH_3 \quad (4)$$

$$Co[(NH)_3]_4^{2+} + 2OH^- \rightarrow Co(OH)_2 + 4NH_3 \quad (5)$$

In the film formation, the NH_3 released from urea was introduced as a complexing agent in the bath and exerted itself to control the release velocity of Ni^{2+} and Co^{2+} ions for deposition of the $Co_xNi_{1-x}(OH)_2$ nanorods.

3.2. Structural Studies. Film crystallinity was analyzed using X-ray diffraction. The XRD patterns of $Co_xNi_{1-x}(OH)_2$ films on GF are shown in Figure 2. The strong diffraction peaks at 2θ of

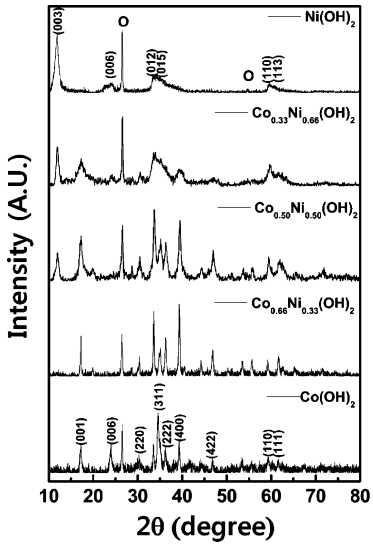

Figure 2. XRD patterns of $Co_xNi_{1-x}(OH)_2$ thin films onto graphene foam substrate at different x compositions.

26.4° and 54.5° in all patterns are attributed to the (002) and (004) reflections of the crystalline peaks of hexagonal graphite carbon, marked as "O" (JCPDS card no 75-1621). The XRD pattern of $Co(OH)_2$ with peaks assigned to (001), (006), (220), (311), (222), (400), (422), (110) and (111) are corresponding to hexagonal mixed phase of α- and β-$Co(OH)_2$ (JCPDS card no. 74-1057)[28] Similarly, XRD of $Ni(OH)_2$ with peaks assigned for (003), (006), (012), (015), (110) and (113) planes correspond to the hexagonal mixed phase of α- and β-$Ni(OH)_2$ (JCPDS card no. 38-0715)[9,29] It is difficult to differentiate between cobalt and nickel hydroxide phases, because they have similar structures and their diffraction peaks are very close. However, at a low angle, the series of (001) and (003) peaks arises from the basal plane reflection of $Co(OH)_2$ and $Ni(OH)_2$ materials, respectively. Along with the basal plan reflection, all diffraction peaks within the range of 10−80° (2θ) attributed to the characteristic reflections of $Co_xNi_{1-x}(OH)_2$ materials. Also, the good crystallinity of the deposited films of $Co_xNi_{1-x}(OH)_2$ materials can be assured by the high and sharper diffraction peaks.

3.3. XPS studies. To obtain more detailed information about elements and oxidation states of the as-prepared

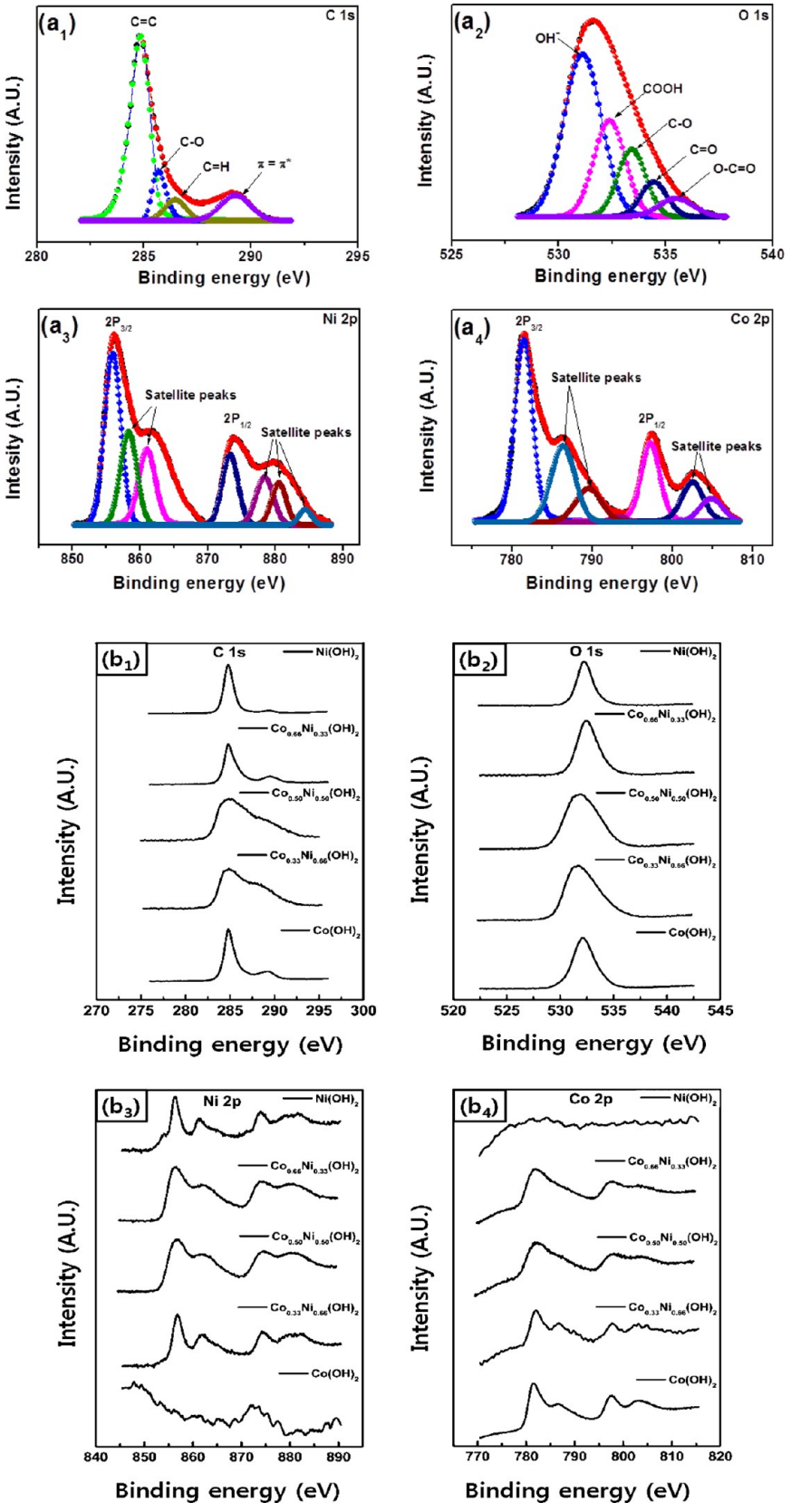

Figure 3. Fitted XPS spectra of (a_1) C 1s, (a_2) O 1s, (a_3) Ni 2p and (a_4) Co 2p for $Co_xNi_{1-x}(OH)_2$/GF electrode and XPS spectra (b_1) C 1s, (b_2) O 1s, (b_3) Ni 2p and (b_4) Co 2p of $Co_xNi_{1-x}(OH)_2$/GF electrodes for all different x compositions.

$Co_xNi_{1-x}(OH)_2$/GF, X-ray photoelectron spectroscopy measurements were performed and the corresponding results are presented in Figure 3. The fitted spectra of C 1s for $Co_xNi_{1-x}(OH)_2$/GF electrode are shown in panels a_{1-4} of Figure 3. Figure 3a_1 reveals that the peak centered at a binding energy of 284.5 eV represents C—C bonding and, along with

dx.doi.org/10.1021/am404863z | ACS Appl. Mater. Interfaces 2014, 6, 2450−2458

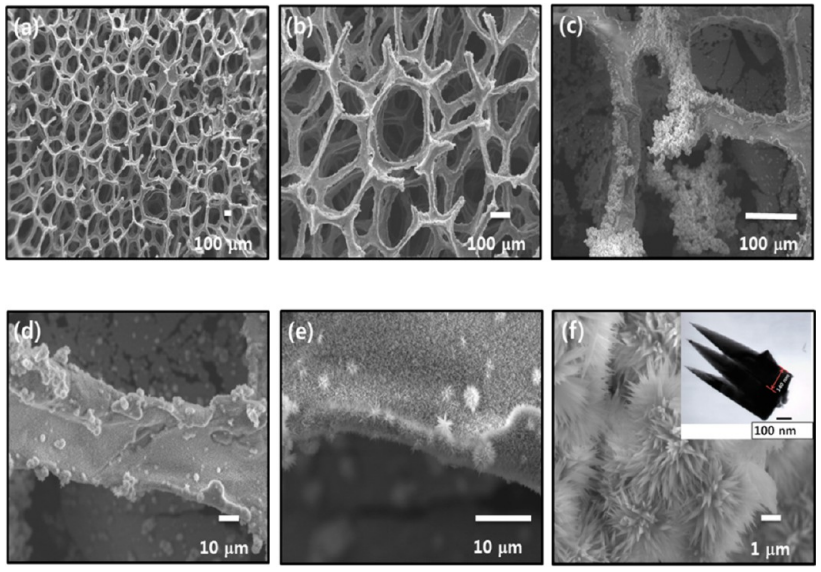

Figure 4. (a-f) SEM micrographs of $Co_xNi_{1-x}(OH)_2$ on the graphene foam at different magnifications. Inset of panel f shows TEM of $Co_xNi_{1-x}(OH)_2$ material.

shoulder peaks at 285, 285.7 and 289.5 eV, can typically be assigned for the C═O, C═H and π═π* surface functional groups.[30] The fitted spectrum for the O 1s region shown in Figure 3a$_2$ reveals oxygen contributions in $Co_xNi_{1-x}(OH)_2$/GF electrode. It is observed that the O 1s core level region is composed of a broad peak centered at 532 eV for all $Co_xNi_{1-x}(OH)_2$ compositions, which is associated with bound hydroxide groups (OH^-) and confirms the $Co_xNi_{1-x}(OH)_2$ formation.[31] The fitting analysis shows that the broad peak consists of weakly adsorbed species such as COOH, C—O, C═O and O—C═O. Thus, XPS studies support the formation of the Co_xNi_{1-x} hydroxide phase on graphene foam. Figure 3a$_3$ shows fitted spectra of Ni 2p for $Co_xNi_{1-x}(OH)_2$/GF electrodes. The Ni 2p spectrum was best fitted by considering two spin−orbit doublets and two shakeup satellites. Two kinds of nickel species have been detected and assigned to species containing Ni^{2+} and Ni^{3+} ions.[32] Specifically, peaks at binding energies (BE) of 853.7 and 871.3 eV are ascribed to Ni^{2+}, whereas the peaks at BE of 855.2 and 872.8 eV are assigned to Ni^{3+}.[32] Similar spin−orbit doublets and shakeup satellite peaks are discernible for Co 2p XPS spectrum (Figure 3a$_4$) including, Co^{3+} ions at BE of 779.5 and 794.6 eV with Co^{2+} ions at 780.8 and 795.9 eV.[33]

Panels b$_{1-4}$ of Figure 3 show that XPS spectra of C 1s, O 1s, Ni 2p and Co 2p for $Co_xNi_{1-x}(OH)_2$/GF electrodes of different x compositions. Figure 3b$_1$ shows similar peaks of C 1s spectra observed for all $Co_xNi_{1-x}(OH)_2$/GF samples, suggesting that graphene surfaces with carboxyl, hydroxyle, epoxy groups are in good connection with $Co_xNi_{1-x}(OH)_2$ for all compositions. The O 1s spectra for all compositions of $Co_xNi_{1-x}(OH)_2$/GF electrodes shown in Figure 3b$_2$ confirms that the hydroxide phase is consistent in all compositions with their peaks centered at 532 eV. Figure 3b$_{3,4}$ reveals spin−orbit doublets and shakeup satellite peaks of Ni 2p and Co 2p for all compositions of $Co_xNi_{1-x}(OH)_2$/GF electrodes. However, Co 2p and Ni 2p spectras are absent in $Ni(OH)_2$/GF and $Co(OH)_2$/GF electrodes. Apparently, the XPS data demonstrates that the surface of the as-prepared $Co_xNi_{1-x}(OH)_2$ sample has a composition containing Co^{2+}, Co^{3+}, Ni^{2+} and Ni^{3+}. Thus, formula of the as-synthesized $Co_xNi_{1-x}(OH)_2$ can generally be expressed as $Co^{2+}{}_xCo^{3+}{}_{1-y}[Ni^{2+}{}_yNi^{3+}{}_{1-x}](OH)_2$ ($0 < x, y < 1$).[34]

3.4. Surface Morphology. The SEM micrographs of the thin $Co_xNi_{1-x}(OH)_2$ film deposited on graphene foam at different magnifications are shown in Figure 4. A wide porous graphene foam skeleton is well-decorated by $Co_xNi_{1-x}(OH)_2$, seen at a low magnification SEM image as shown in Figure 4a. Figure 4b,c shows that the overgrowth of $Co_xNi_{1-x}(OH)_2$ on twigs of graphene foam is well-covered with overgrowth. This overgrowth can be attributed to the nucleation and coalescence process. Surface morphology in Figure 4d,e reveals that the graphene sheet of ∼25−30 μm in width with edges are well-covered by the nanorods of $Co_xNi_{1-x}(OH)_2$. The high magnification SEM image (Figure 4f) demonstrates that these nanorods are ∼0.9 μm in length with a width of ∼140−180 nm. TEM image shown in inset of Figure 4f reveals needlelike shaped nanorods with a sharp tip having a size of about ∼140 nm. Such nanorod-like morphology leads to a high specific surface area with better diffusion path, which provides the structural foundation for the high specific capacitance.[35]

Figure 5 shows the SEM images of $Co_xNi_{1-x}(OH)_2$/GF with an increase of Nickel content. Figure 5a,b shows SEM images of $Co(OH)_2$/GF at different magnifications. Figure 5b shows a vertically aligned nanorod-like structure with a $Co(OH)_2$ size of about ∼160−180 nm. The SEM images of $Co_xNi_{1-x}(OH)_2$ for composition 0.66:0.33 (Co:Ni) shown in Figure 5c,d reveals a similar nanorod-like structure. Interestingly, the size of rods is reduced and found to be in the range of ∼125−140 nm. The size of the nanorods for $Co_xNi_{1-x}(OH)_2$ with composition 0.5:0.5 (Co:Ni) was further reduced and found to be ∼50−80 nm (shown in Figure 5e,f). Furthermore, nanorods were found with a small size about ∼35−45 nm, as shown in Figure 5g,h for the 0.33:0.66 composition of Co:Ni. However, the fuzzy morphology composed from nanoparticles is observed for $Ni(OH)_2$, shown in Figure 5i,j. The SEM analysis reveals that nanorods of $Co(OH)_2$ reduce in size from 180 to 35 nm with increases in nickel content and are converted into the $Ni(OH)_2$ fuzzy nanoparticle structure. Also, such transformation in the micro-flake-like structure of $Co_xNi_{1-x}(OH)_2$ LDH with increased Ni content has been reported by Kulkarni et al.[15] The $Co_xNi_{1-x}(OH)_2$ demonstrates composition-dependent micro-structures with randomly grown nanorod-like morphology.

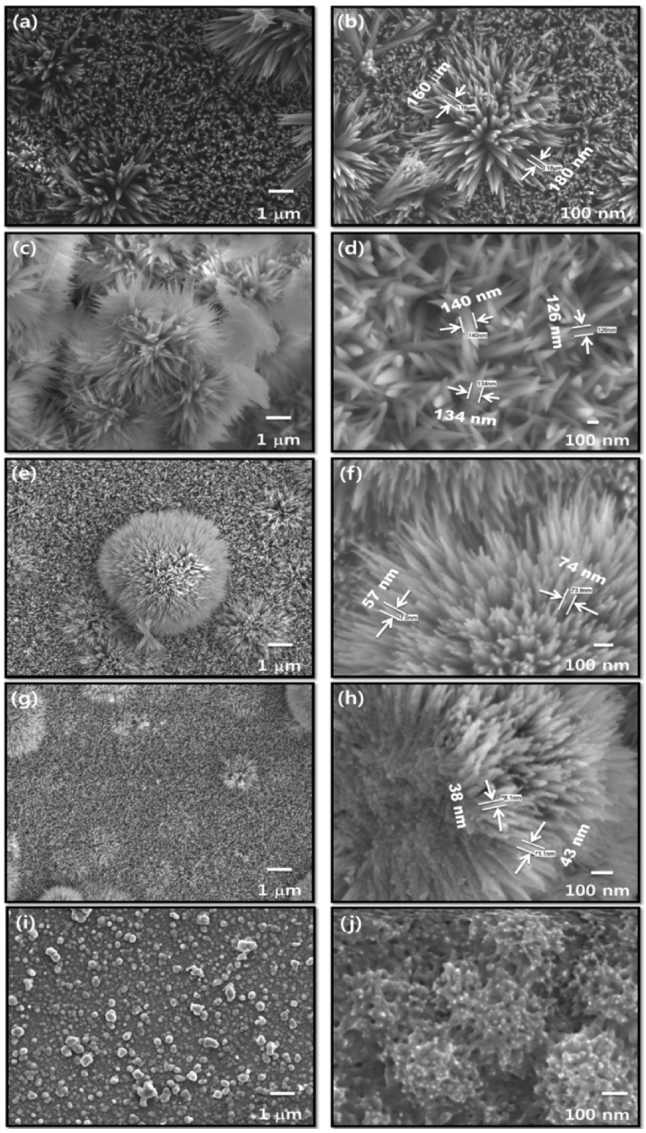

Figure 5. SEM images of $Co_xNi_{1-x}(OH)_2$ at different magnifications with increases in Ni content from $Co(OH)_2$ to $Ni(OH)_2$ vertically grown nanorods for $Co_xNi_{1-x}(OH)_2$ (a, b) $x = 1$ (~160−180 nm), (c, d) $x = 0.66$ (~125−140 nm), (e, f) $x = 0.50$ (~50−80 nm), (g, h) $x = 0.33$ (~35−45 nm) and (i, j) $x = 0$, i.e., fuzzy nanostructure.

Consequently, the results imply that the content of Ni in $Co_xNi_{1-x}(OH)_2$ alters the surface morphological properties of $Co_xNi_{1-x}(OH)_2$ electrodes. The highly oriented nanorod microstructure of $Co_xNi_{1-x}(OH)_2$ is a potential structure for supercapacitor applications; it provides a large surface area with a loosely packed structure, which offers proficient pathways to electrolyte ions and charges to enhance the capacitive performance. The elemental composition from energy-dispersive X-ray spectroscopy (EDS) analysis attributes the presence of both $Co(OH)_2$ and $Ni(OH)_2$ in $Co_xNi_{1-x}(OH)_2$ (shown in Figure S3, (see the Supporting Information)). From EDS analysis, $Co_xNi_{1-x}(OH)_2$ with $x = 0.66$, 0.50 and 0.33 reveals the Co:Ni composition as 2.01:1, 1:1.2 and 2.07:1, respectively.

3.5. Supercapcitive Studies. The electrochemical measurements for supercapacitor were carried out in a three electrode electrochemical cell in which the $Co_xNi_{1-x}(OH)_2$/GF electrode was used as a working electrode, platinum as a counter and Ag/AgCl as a reference electrode. Typical cyclic voltammograms (CV) of the $Co_xNi_{1-x}(OH)_2$/GF electrode for different x (Ni) values ($x = 0.0$ to 1) in an aqueous 1 M KOH electrolyte solution at a sweep rate of 50 mV s^{-1} within an optimized potential range of −0.2 to +0.5 V is shown in Figure 6a. All the curves display two

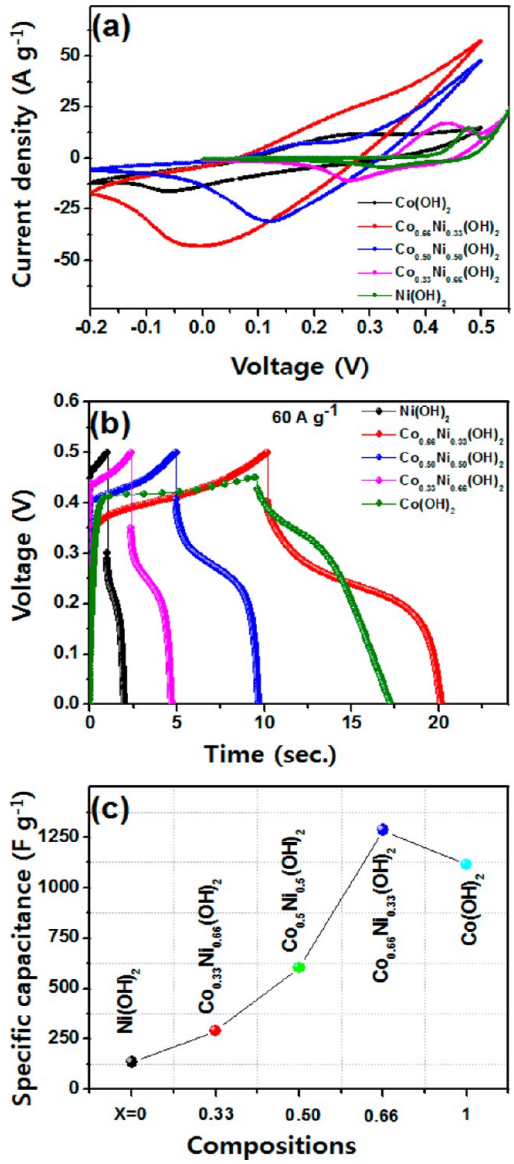

Figure 6. Electrochemical studies of $Co_xNi_{1-x}(OH)_2$/GF with various x compositions. (a) Cyclic voltammograms within optimized potential range of −0.2 to +0.5 V in aqueous 1 M KOH at a scan rate of 50 mV s^{-1}. (b) Galvanostatic charge−discharge (GCD) plots within potential window of 0 to 0.5 V at constant charging current of 60 A g^{-1}. (c) Graph of Ni:Co composition dependent (x) specific capacitance.

prominent characteristic redox peaks, which specify the pseudocapacitive behavior. Generally, an ideal capacitor exhibits a rectangular shaped CV curve; however, the two prominent redox peaks, which occur within the voltage range, are typical signs of a pseudocapacitive behavior.[36] The $Co(OH)_2$/GF, $Ni(OH)_2$/GF and $Co_xNi_{1-x}(OH)_2$/GF electrodes showed very strong redox peaks due to the following Faradaic reactions of $Co(OH)_2$ and $Ni(OH)_2$,

$$Co(OH)_2 + OH^- \rightarrow CoOOH + H_2O + e^- \quad (6)$$

dx.doi.org/10.1021/am404863z | ACS Appl. Mater. Interfaces 2014, 6, 2450−2458

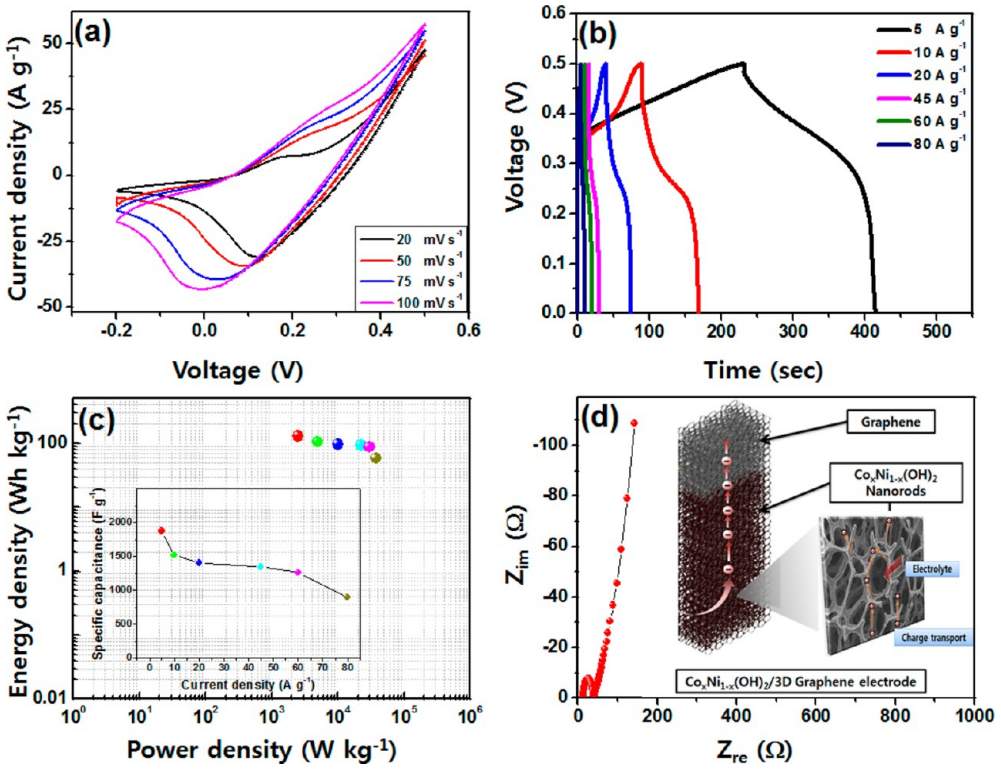

Figure 7. (a) Voltammetric responses of $Co_{0.66}Ni_{0.33}(OH)_2$/GF electrode at different scan rates. (b) Galvanostatic charge–discharge cycling of $Co_{0.66}Ni_{0.33}(OH)_2$/GF in 1 M KOH solution at different current densities from 5 to 80 A g^{-1}. (c) Ragone plot for $Co_{0.66}Ni_{0.33}(OH)_2$/GF at different current densities. Inset shows graph of specific capacitance with different current densities. (d) Nyquist plots of $Co_{0.66}Ni_{0.33}(OH)_2$/GF electrodes over the frequency range of 10 MHz to 0.01 Hz. Inset shows schematic mechanism of 3D graphene foam as current collector with high surface area to improve the electrochemical performance of $Co_xNi_{1-x}(OH)_2$.

$$Ni(OH)_2 + OH^- \rightarrow NiOOH + H_2O + e^- \quad (7)$$

The CV curves showed shifts in the redox peaks as the compositions of the $Co_xNi_{1-x}(OH)_2$ are changed. The CV curves reveal that the voltage values of oxidation and reduction peaks get shifted toward the more positive side with increased Ni content in $Co_xNi_{1-x}(OH)_2$/GF. The oxidation and reduction peaks for the $Co(OH)_2$/GF are at 0.25 and −0.065 V, whereas for the $Ni(OH)_2$/GF, the peaks are observed at 0.47 and 0.33 V, respectively. The measured capacitance for all CV curves is mainly based on redox mechanism arises from quasi-reversible electron transfer. As compared with those of the pure $Ni(OH)_2$/GF and $Co(OH)_2$/GF electrodes, $Co_xNi_{1-x}(OH)_2$/GF showed a much more standardized distribution of current under the curve. Such an obtained result might be due to the binary metal combining as a hydroxide material for supercapacitor application; which offers feasible oxidation states along with an ideally mutated structure.[37] The maximal integral area and redox current is obtained for $Co_{0.66}Ni_{0.33}(OH)_2$/GF electrode.

Figure 6b shows galvanostatic charge–discharge (GCD) plots of $Co_xNi_{1-x}(OH)_2$/GF within potential window of 0 to 0.5 V at a constant charging current of 60 A g^{-1}. The $Co(OH)_2$/GF electrode shows a smaller potential charge–discharge window of about 0 to 0.45 V than other $Co_xNi_{1-x}(OH)_2$/GF electrodes. The nonlinear charge–discharge profile of the $Co_xNi_{1-x}(OH)_2$/GF electrode arises from the redox reaction, which deviates from usual linear behavior of voltage with time, normally exhibited by EDLCs.[38] Figure 6c shows graph of specific capacitance with different Ni:Co compositions. Solitary $Co(OH)_2$/GF shows higher capacitance than that of solitary $Ni(OH)_2$/GF, and the combined supercapacitance of $Co_{0.66}Ni_{0.33}(OH)_2$/GF is higher than that of individual $Ni(OH)_2$/GF and $Co(OH)_2$/GF. The $Co_{0.66}Ni_{0.33}(OH)_2$/GF is found to be an appropriate combination of $Co_xNi_{1-x}(OH)_2$/GF, which showed a maximum supercapacitance of 1280 F g^{-1} at a charging current density of 60 A g^{-1}.

The voltammetric responses of the $Co_{0.66}Ni_{0.33}(OH)_2$/GF electrode at different scan rates, from 20 to 100 mV s^{-1}, are shown in Figure 7a. It is observed that the current under curve is gradually increased with a higher scan rate and hence signifies an ideally capacitive behavior. The $Co_{0.66}Ni_{0.33}(OH)_2$/GF electrode is used for galvanostatic charge–discharge cycling between 0 and 0.5 V in 1 M KOH electrolyte at different current densities, from 5 to 80 A g^{-1}, shown in Figure 7b. An increase in the IR drop with an increase in the charging current density for $Co_{0.66}Ni_{0.33}(OH)_2$/GF electrode is clearly observed. The relation between current density dependent the specific capacitance with $Co_{0.66}Ni_{0.33}(OH)_2$/GF electrode shows a decrease in specific capacitance from 1847 to 869 F g^{-1} with increases in current density (shown in inset of Figure 7c). It is observed that a rise in charging current density decreases specific capacitance values. This is a consequence of the diffusion effect of the proton within the electrode, where inner active sites cannot precede the redox transitions completely at a higher current density.[39] Energy and power densities were calculated from the galvanostatic charge–discharge, with current densities of 5 to 80 A g^{-1}, are used in the Ragone plot shown in Figure 7c. The maximum power density and energy density for $Co_{0.66}Ni_{0.33}(OH)_2$/GF electrode are found to be 10 kW kg^{-1} and 62 Wh kg^{-1}, respectively. Galvanostatic charge–discharge cyclic stability is studied for $Co_{0.66}Ni_{0.33}(OH)_2$/GF electrode over 1000 cycles at 80 A g^{-1}

(shown in Figure S4 (see the Supporting Information)). The capacitance is decreased by 25% up to 900 cycles and thereafter dropped by 36% for 1000 cycles, at current density 80 A g^{-1}. Hence, the stability of electrode retained to ~75% up to 900th cycles and later drastic decrement of 11% is observed for next 100 cycles.

Figure 7d presents the complex plane electrochemical impedance spectra (EIS) of the $Co_{0.66}Ni_{0.33}(OH)_2$/GF electrode. The EIS measurements were carried out by measuring the open circuit potential (OCP) over the frequency range of 10 MHz to 0.01 Hz. A sharp increase of the imaginary part of the EIS at lower frequencies is due to the capacitive behavior of the electrodes, where a semicircular loop at higher frequencies is due to charge-transfer resistance (R_{ct}). The R_{ct} can be calculated from the diameter of the initial curvature at higher frequencies.[40] The solution resistance (R_s) and R_{ct} of the $Co_{0.66}Ni_{0.33}(OH)_2$/GF electrode are found to be 0.35 and 80 Ω, respectively. The $Co_xNi_{1-x}(OH)_2$/GF electrode offers many advantages over the conventionally used $Co_xNi_{1-x}(OH)_2$ electrodes in supercapacitors. Generally, graphene−$Co_xNi_{1-x}(OH)_2$ composites with surface-anchored, layer-by-layer assembled and randomly mixed architectures have been utilized as advanced electrode materials for supercapacitors.[41−43] Such conventional architectures offer self-dimensional restrictions in charge transportation during charge−discharge process. However, herein we presented effective utilization of $Co_xNi_{1-x}(OH)_2$ nanorods anchored on lightweight 3D graphene foam and as supercapacitor electrodes. In such a structure, the 3D graphene foam serves as the current collector with high surface area and improves the electron conductivity to effectively utilize $Co_xNi_{1-x}(OH)_2$ nanorods for a low diffusion path (schematic mechanism shown in inset of Figure 7d). Also, the hierarchical one-dimensional nanostructures of $Co_{0.66}Ni_{0.33}(OH)_2$ on the 3D graphene foam possess a large surface area with a porous structure, which allows them to interact effectively with the electrolyte ions.

A rough comparison of the obtained specific capacitance at particular current density, energy and power density in a typical Ragone plot, with some recent reports, is shown in Figure 8a,b. Figure 8a shows that the power density at moderate energy density obtained in the present work surpasses previous literature values reported for aqueous electrolyte based $Co_xNi_{1-x}(OH)_2$ supercapacitors.[15,19,22,42] Though the obtained maximum specific capacitance is higher than that reported for pure $Co_xNi_{1-x}(OH)_2$ and different graphene−$Co_xNi_{1-x}(OH)_2$ composites, as shown in Figure 8b,[11,20−22,43−46] with the exception of electrodeposited $Co_xNi_{1-x}(OH)_2$ on the Ni foam electrode.[44] However, the $Co_xNi_{1-x}(OH)_2$/GF electrode is lighter than $Co_xNi_{1-x}(OH)_2$ on the Ni foam, which subsequently can offer an industrial application in energy storage devices.

4. CONCLUSIONS

The nanostructured porous $Co_xNi_{1-x}(OH)_2$/GF electrodes, which exhibit both $Co(OH)_2$ and $Ni(OH)_2$, are successfully synthesized by the CBD method, showing randomly oriented nanorod-like morphologies. The increase of Ni content (x = 0, 0.33, 0.50, 0.66 and 1) in $Co_xNi_{1-x}(OH)_2$/GF affects the emerging surface morphological aspect. The maximal specific capacitance for the $Co_xNi_{1-x}(OH)_2$/GF electrode is found to be 1847 F g^{-1}, attaining a specific energy of 62 Wh kg^{-1} and a specific power of 10 kW kg^{-1} for the composition $Co_{0.66}Ni_{0.33}(OH)_2$/GF in 1 M KOH electrolyte. It is demonstrated that $Co_{0.66}Ni_{0.33}(OH)_2$ nanorods can achieve a high specific capacitance by applying the graphene foam as a conducting 3D network. The simple synthetic approach may provide a convenient route for the preparation of $Co_xNi_{1-x}(OH)_2$/GF as an efficient electrode in a high energy storage application. As per the requirement of devices (high energy or power), $Co_xNi_{1-x}(OH)_2$/GF electrodes can be employed in asymmetric, nonaqueous and solid state devices.

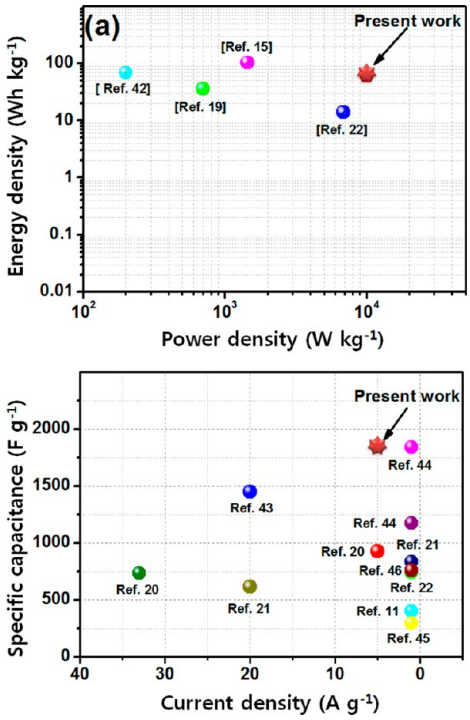

Figure 8. Comparative (a) Ragone plot of energy and power density and (b) specific capacitance at 5 A g^{-1} for $Co_{0.66}Ni_{0.33}(OH)_2$/GF based ECs with other reported references.

■ ASSOCIATED CONTENT

Ⓢ Supporting Information

Schematic diagram of preparation procedure for 3D interconnected graphene foam (Figure S1), weight of $Co_xNi_{1-x}(OH)_2$ deposited material on GF electrode after 4 h of deposition (Figure S2), EDS elemental analysis spectra (Figure S3) and cyclic stability of $Co_{0.66}Ni_{0.33}(OH)_2$/GF electrode for 1000 cycles (Figure S4). This material is available free of charge via the Internet at http://pubs.acs.org.

■ AUTHOR INFORMATION

Corresponding Author

*Seong Chan Jun. Address: Nano ElectroMechanical Device Laboratory, School of Mechanical Engineering, Yonsei University, Seoul 120-749, South Korea. Tel: +82-2-2123-5817. Fax: +82-2-312-2159. E-mail: scj@yonsei.ac.kr.

Author Contributions

§Equally contributing authors: Umakant M. Patil and Ji Soo Sohn.

Notes

The authors declare the following competing financial interests.

■ ACKNOWLEDGMENTS

This work was partially supported by the Pioneer Research Center Program (2010-0019313), and the Priority Research Centers Program (2009-0093823) through the National

Research Foundation (NRF) of Korea funded by the Ministry of Science, ICT & Future Planning.

REFERENCES

(1) Wang, G.; Zhang, L.; Zhang, J. *Chem. Soc. Rev.* **2012**, *41*, 797−828.
(2) Miller, J. R.; Simon, P. *Science* **2008**, *321*, 651−652.
(3) Conway, B. *Electrochemical supercapacitors: scientific fundamentals and technological applications (POD)*; Kluwer Academic/Plenum: New York, 1999.
(4) Halper, M. S.; Ellenbogen, J. C. *Supercapacitors: A Brief Overview*; Report No. MP 05W0000272; The MITRE Corporation: McLean, VA, 2006; pp 1−34.
(5) Etacheri, V.; Marom, R.; Elazari, R.; Salitra, G.; Aurbach, D. *Energy Environ. Sci.* **2011**, *4*, 3243−3262.
(6) Zhang, L. L.; Zhao, X. *Chem. Soc. Rev.* **2009**, *38*, 2520−2531.
(7) Li, N.; Cao, M.; Hu, C. *Nanoscale* **2012**, *4*, 6205−6218.
(8) Hu, C.-C.; Chen, W.-C. *Electrochim. Acta* **2004**, *49*, 3469−3477.
(9) Patil, U.; Gurav, K.; Fulari, V.; Lokhande, C.; Joo, O. S. *J. Power Sources* **2009**, *188*, 338−342.
(10) Gao, Z.; Yang, W.; Yan, Y.; Wang, J.; Ma, J.; Zhang, X.; Xing, B.; Liu, L. *Eur. J. Inorg. Chem.* **2013**, *2013*, 4832−4838.
(11) Yuan, C.; Li, J.; Hou, L.; Yang, L.; Shen, L.; Zhang, X. *J. Mater. Chem.* **2012**, *22*, 16084−16090.
(12) Liu, T.; Xu, S.; Wang, L.; Chu, J.; Wang, Q.; Zhu, X.; Bing, N.; Chu, P. K. *J. Mater. Chem.* **2011**, *21*, 19093−19100.
(13) Su, L.; Gong, L.; Gao, J. *J. Power Sources* **2012**, *209*, 141−146.
(14) Hu, Z.-A.; Xie, Y.-L.; Wang, Y.-X.; Wu, H.-Y.; Yang, Y.-Y.; Zhang, Z.-Y. *Electrochim. Acta* **2009**, *54*, 2737−2741.
(15) Kulkarni, S. B.; Jagadale, A. D.; Kumbhar, V. S.; Bulakhe, R. N.; Joshi, S. S.; Lokhande, C. D. *Int. J. Hydrogen Energy* **2013**, *38*, 4046−4053.
(16) Deng, S.; Sun, D.; Wu, C.; Wang, H.; Liu, J.; Sun, Y.; Yan, H. *Electrochim. Acta* **2013**, *111*, 707−712.
(17) Rajeswari, J.; Kishore, P. S.; Viswanathan, B.; Varadarajan, T. K. *Electrochem. Commun.* **2009**, *11*, 572−575.
(18) Zhang, G.; Lou, X. W. *Sci. Rep.* **2013**, *3*, 1−6.
(19) Ghosh, D.; Giri, S.; Das, C. K. *ACS Sustainable Chem. Eng.* **2013**, *1*, 1135−1142.
(20) Carriazo, D.; Patino, J.; Gutierrez, M. C.; Ferrer, M. L.; del Monte, F. *RSC Adv.* **2013**, *3*, 13690−13695.
(21) Wang, H.-W.; Hu, Z.-A.; Chang, Y.-Q.; Chen, Y.-L.; Wu, H.-Y.; Zhang, Z.-Y.; Yang, Y.-Y. *J. Mater. Chem.* **2011**, *21*, 10504−10511.
(22) Jiang, H.; Ma, J.; Li, C. *Chem. Commun.* **2012**, *48*, 4465−4467.
(23) Ji, J.; Zhang, L. L.; Ji, H.; Li, Y.; Zhao, X.; Bai, X.; Fan, X.; Zhang, F.; Ruoff, R. S. *ACS Nano* **2013**, *7*, 6237−6243.
(24) Chen, Z.; Ren, W.; Gao, L.; Liu, B.; Pei, S.; Cheng, H.-M. *Nat. Mater.* **2011**, *10*, 424−428.
(25) Dong, X.-C.; Xu, H.; Wang, X.-W.; Huang, Y.-X.; Chan-Park, M. B.; Zhang, H.; Wang, L.-H.; Huang, W.; Chen, P. *ACS Nano* **2012**, *6*, 3206−3213.
(26) Hodes, G. *Phys. Chem. Chem. Phys.* **2007**, *9*, 2181−2196.
(27) Zhao, Y.; Wang, J.; Chen, H.; Pan, T.; Zhang, J.; Cao, C. *Electrochim. Acta* **2004**, *50*, 91−98.
(28) Jagadale, A. D.; Kumbhar, V. S.; Dhawale, D. S.; Lokhande, C. D. *Electrochim. Acta* **2013**, *98*, 32−38.
(29) Wang, Y.-x.; Hu, Z.-a.; Wu, H.-y. *Mater. Chem. Phys.* **2011**, *126*, 580−583.
(30) Yang, D.; Velamakanni, A.; Bozoklu, G.; Park, S.; Stoller, M.; Piner, R. D.; Stankovich, S.; Jung, I.; Field, D. A.; Ventrice, C. A., Jr *Carbon* **2009**, *47*, 145−152.
(31) Dupin, J.-C.; Gonbeau, D.; Vinatier, P.; Levasseur, A. *Phys. Chem. Chem. Phys.* **2000**, *2*, 1319−1324.
(32) Grosvenor, A. P.; Biesinger, M. C.; Smart, R. S. C.; McIntyre, N. S. *Surf. Sci.* **2006**, *600*, 1771−1779.
(33) Shim, H.-S.; Shinde, V. R.; Kim, H. J.; Sung, Y.-E.; Kim, W. B. *Thin Solid Films* **2008**, *516*, 8573−8578.
(34) Kim, J.-G.; Pugmire, D.; Battaglia, D.; Langell, M. *Appl. Surf. Sci.* **2000**, *165*, 70−84.
(35) Lee, J. W.; Hall, A. S.; Kim, J.-D.; Mallouk, T. E. *Chem. Mater.* **2012**, *24*, 1158−1164.
(36) Zhi, M.; Xiang, C.; Li, J.; Li, M.; Wu, N. *Nanoscale* **2013**, *5*, 72−88.
(37) Yang, F.; Yao, J.; Liu, F.; He, H.; Zhou, M.; Xiao, P.; Zhang, Y. *J. Mater. Chem. A* **2013**, *1*, 594−601.
(38) Li, J.; Yang, M.; Wei, J.; Zhou, Z. *Nanoscale* **2012**, *4*, 4498−4503.
(39) Orazem, M. E.; Tribollet, B. *Electrochim. Acta* **2008**, *53*, 7360−7366.
(40) Lasia, A. *Electrochemical Impedance Spectroscopy and its Applications*; Kluwer Academic/Plenum Publishers: New York, 1999.
(41) Huang, L.; Chen, D.; Ding, Y.; Feng, S.; Wang, Z. L.; Liu, M. *Nano Lett.* **2013**, *13*, 3135−3139.
(42) Salunkhe, R. R.; Jang, K.; Lee, S.-w.; Yu, S.; Ahn, H. *J. Mater. Chem.* **2012**, *22*, 21630−21635.
(43) Yuan, C.; Li, J.; Hou, L.; Zhang, X.; Shen, L.; Lou, X. W. D. *Adv. Funct. Mater.* **2012**, *22*, 4592−4597.
(44) Chang, J.; Sun, J.; Xu, C.; Xu, H.; Gao, L. *Nanoscale* **2012**, *4*, 6786−6791.
(45) Wu, T.; Li, J.; Hou, L.; Yuan, C.; Yang, L.; Zhang, X. *Electrochim. Acta* **2012**, *81*, 172−178.
(46) Wang, H.; Gao, Q.; Jiang, L. *Small* **2011**, *7*, 2454−2459.